Materials Advances

ROYAL SOCIETY OF CHEMISTRY

PAPER

View Article Online
View Journal | View Issue

Check for updates

Cite this: *Mater. Adv.*, 2024, 5, 8265

A dual functional Cu(II)-coordination polymer and its rGO composite for selective solvent detection and high performance energy storage†

Basree,‡[a] Waris,[bc] Arif Ali,‡[d] Nishat Khan,[a] Mohammad Zain Khan,[c] Ganesh Chandra Nayak,[d] Kafeel Ahmad Siddiqui *[e] and Musheer Ahmad *[a]

Received 28th July 2024,
Accepted 26th August 2024

DOI: 10.1039/d4ma00762j

rsc.li/materials-advances

Herein, the fabrication of a new Cu(II)-based coordination polymer $\{[Cu_2(DPP)_2(H_2O)_2]\cdot DPP\cdot 2NO_3\}_n$ (**CP-1**) (DPP = 1,3-di(4-pyridyl)propane) and its composite (**rGO@CP-1**) has been done using solvothermal and mechanochemical methods. The crystal structure of the synthesized **CP-1** was confirmed utilizing single-crystal X-ray diffraction (SC-XRD). Furthermore, the structural features of the as-synthesized **CP-1** and **rGO@CP-1** were examined using PXRD, FTIR, TGA, SEM, and HR-TEM analysis. The topological framework of **CP-1** shows a ***1,3M4-1*** underlying net for two fragments and the hydrogen-bonded network shows a ***2C1*** underlying net topology. The fluorescence detection of transition metal ions and solvents using **CP-1** showed promising results of 97.4% DMF and 96.8% Zn^{2+}. Electrochemical study of **CP-1** and **rGO@CP-1** was performed in an acidic medium (1 M H_2SO_4) electrolyte utilizing cyclic voltammetry (CV) and galvanostatic charge–discharge (GCD) techniques with a specific capacity of 244.17 F g^{-1} and 899.54 F g^{-1} for **CP-1** and **rGO@CP-1**, respectively at 1 A g^{-1} (current density). Moreover, 98.6% columbic efficiency with 94.62% capacity retention of **rGO@CP-1** was obtained at 8 A g^{-1} up to 2000 cycles.

1. Introduction

In this digital era, the challenges of power generation, energy storage, and global climate change necessitate a range of technologically advanced solutions to address the contradiction between fossil resource consumption and environmental preservation.[1] There has been a dramatic increase in the need for readily accessible, portable electrical and rechargeable devices in recent years.[2–4] Therefore, scientists have created energy storage systems that are affordable, versatile, and highly effective in order to meet these increasing demands. Electrochemical energy storage systems that use supercapacitors (SCs) as anodes (redox-type) and cathodes (capacitive qualities) have shown great promise.[5–8] Recent literature on supercapacitors (SCs) has shown their potential as superlative energy storage and power storage sources for electrical and battery-type vehicles.[9–11] The SCs demonstrate outstanding electrochemical performance, including higher power density, fast charge–discharge rate, and long-term lifespan. The exceptional energy storage properties of SCs are mainly influenced by the properties of the electrode material, including its shape adjustability, high electrochemical activity, excellent mechanical and chemical properties, specific surface area, adjustable porosity, and strong conductivity.[12–15] Therefore, coordination polymers are highly favored for SC applications due to their ability to meet all the necessary SC features.

In this scenario, CPs are materials that have a highly crystalline structure, consisting of central metal ions or metal clusters connected by organic linkers.[16–18] Due to the advantages of CPs, such as adjustable porosity, tunable chemical structure, and controllable morphology, CPs have been used for a wide range of applications, such as adsorption,[19–22] separation,[19] catalysis,[23] gas storage, drug delivery,[24] luminescence sensing,[25,26] waste-water treatment,[27] batteries,[2] and more recently, supercapacitors.[28]

Accurately detecting trace elements in environmental and biological processes continues to be a major challenge, requiring the use of appropriate sensors.[29] Zinc (Zn^{2+}) is the most

[a] *Department of Applied Chemistry, ZHCET, Faculty of Engineering and Technology, Aligarh Muslim University Aligarh, UP, 202002, India. E-mail: amusheer4@gmail.com*
[b] *Environmental Research Laboratory, Department of Chemistry, Faculty of Science, Aligarh Muslim University Aligarh, UP, 202002, India*
[c] *Electrochemical Research Laboratory, Department of Industrial Chemistry, Faculty of Science, Aligarh Muslim University Aligarh, UP, 202002, India*
[d] *Department of Chemistry & Chemical Biology, Indian Institute of Technology (ISM), Dhanbad–826004, Jharkhand, India*
[e] *Department of Chemistry, National Institute of Technology Raipur, Great Eastern Road, Raipur, Chhattisgarh, 492010, India. E-mail: kasiddiqui.chy@nitrr.ac.in*

† Electronic supplementary information (ESI) available. CCDC 2314704. For ESI and crystallographic data in CIF or other electronic format see DOI: https://doi.org/10.1039/d4ma00762j

‡ Basree and A. Ali contributed equally to the article.

Open Access Article. Published on 01 October 2024. Downloaded on 2/13/2026 7:18:18 AM. This article is licensed under a Creative Commons Attribution-NonCommercial 3.0 Unported Licence.

Open Access Article. Published on 01 October 2024. Downloaded on 2/13/2026 7:18:18 AM. This article is licensed under a Creative Commons Attribution-NonCommercial 3.0 Unported Licence.

abundant metal ion among all the transition elements in the human body, following Fe^{3+}. The Zn^{2+} ion is crucial for various functions in the human body, including gene expression, neural signal transmission, cell apoptosis, and pathological processes.[30–32] It is important to maintain a balanced level of Zn^{2+} for optimal human health.[33] Furthermore, an overabundance of Zn^{2+} ions can result in a decrease in soil microbial activity due to the influence of plant toxins. On the other hand, volatile organic compounds such as EtOH, DMSO, TEA and DMF are non-biodegradable and constitute a lasting hazard to human health.[34] Keeping in mind both human health and environmental concerns, it is crucial to develop extremely effective techniques for the prompt and accurate detection of Zn^{2+} and organic volatile chemicals (DMF). As a result, developing novel fluorescence sensors capable of selectively sensing Zn^{2+} ions as well as organic volatile compounds with increased sensitivity is essential in current progress. Nowadays, florescence-based CPs have gained a lot of attention due to selectivity, operability simplicity and sensitivity.[35,36]

Zhao *et al.* reported the high-performance sensing of Fe^{3+} ions using a chiral lanthanide-based CP with 99.06% detection limit.[37] MIL-53-L5 (L5 = 2-(pyrene-1-imine) terephthalic acid) nanocrystals have been reported for the sensing of a trace amount of Cu^{2+} in aqueous solution with a good K_{sv} value of 6.15×10^3.[38] Xu *et al.* fabricated the $[Eu(BTB)(phen)](DMF)_{4.5}(H_2O)_2$ CP structure and checked the luminescence sensing of Al^{3+} ions with 5×10^{-8} M (1.35 ppb) detection limit.[39]

The ultrahigh specific surface area, high porosity, and structural tunability of CPs give them excellent electrochemical performance, and better lifespan, power density, and charging–discharging rates. However, CPs have not shown good conductivity. In contrast, reduced graphene oxide has good conducting nature and high surface area, thus showing many advantages to enhance the conductivity of CPs. Banerjee *et al.* have reported a Ni-doped MOF/**rGO** composite which has shown a specific capacitance of 758 F g^{-1}.[40] Deka *et al.* reported a 2D layered CP of Ni(II) for a supercapacitor with a specific capacitance of 802 F g^{-1} at 3 A g^{-1} current density and good cycling stability up to ~95% at 5000 cycles.[41] Ghosh *et al.* synthesized a Zn(II)-based 1D CP by using the slow diffusion method and its hetero nanocomposite (Zn–CP/**rGO**) by an ultrasonication approach with a specific capacitance of 261 F g^{-1} and 377 F g^{-1} at 1 A g^{-1} current density and the retention stability of 97% and 85% at 6 A g^{-1} upon 6000 charging–discharging cycles, respectively.[42] Cai *et al.* reported a Ni(II)-based 1D π–d conjugated CP, namely (Ni-BTA), for energy storage functions with high coloration efficiency (223.6 cm^2 C^{-1}), with a high gravimetric capacity of 168.1 mA h g^{-1} and high retention durability for 10 k cycles.[43] Gupta *et al.* fabricated 2D Cu-MOF and composite (Cu-MOF/**rGO**) by solvothermal and ultrasonication methods to develop an electrode material for energy storage applications with a specific capacitance of 462 F g^{-1} for Cu-MOF and 256 F g^{-1} for Cu-MOF/**rGO** at 0.8 A g^{-1}, and the cyclic stability was 77.7% and 93.75% at 12 A g^{-1} current density upon 1000 cycles, respectively.[44]

As per the literature, several types of CPs/MOFs (1D to 3D) have been reported for energy storage applications. Several CPs that are reported in the literature have similar structures to our synthesized **CP-1**. For instance, Stone *et al.* fabricated three different copper malonate coordination polymers containing dpp linkers which showed rare 2D + 1D + 1D = 3D topology with different structures.[45] The structure of these polymers is mainly influenced by the steric bulk of malonate linkers. YU *et al.* developed two novel one-dimensional Cu(II)-based coordination polymers containing H_2bpdc = biphenyl-4,4′-dicarboxylic acid, bpp = 1,3-di(4-pyridyl)propane and H_2tdc = thiophene-2,5-dicarboxylic acid organic linkers.[46] In both the complexes, the conformation of the bpp ligand is different. Luo *et al.* synthesized two unique Cu(II)-based coordination polymers having bpp = 1,3-bis(4-pyridyl)propane, tp = terephthalate, ip = isophthalate organic linkers.[47] The electrochemical study revealed that both the complexes have oxidizable/reducible properties. Herein, we reported a 1D Cu(II)-based coordination polymer (**CP-1**) for the detection of metal ions (Co, Cd, Fe and Zn) as well as solvent (EtOH, DMSO, H_2O, TEA and DMF) analytes. The fabricated **CP-1** showed good selective detection towards the Zn^{2+} ion with 96.8% and DMF with 97.4%, and these results were obtained in triplicate. The **CP-1** and **rGO@CP-1** showed better electrochemical energy storage with specific capacity of 244.17 F g^{-1} and 899.54 F g^{-1} for **CP-1** and **rGO@CP-1**, respectively, at 1 A g^{-1} (current density) with a retention stability of **rGO@CP-1** of 94.62% up to 2000 cycles. However, **rGO@CP-1** has better cycling stability as compared to the as-synthesized electrode material of **CP-1**. The composite material could be used as a promising electrode material for energy storage applications.

2. Experimental section

2.1 Reagents and materials

1,3-Di(4-pyridyl)propane (DPP) and copper nitrate trihydrate $[Cu(NO_3)_2{\cdot}3H_2O]$ were procured from Sigma-Aldrich with analytical grade (AR/ACS). All solvents and NaOH were purchased from Thermo Fisher Scientific, India. Also, all the other chemicals were purchased from Thermo Fisher Scientific with AR grade, India, and used without further purification.

2.2 Methods and instrumentation

FTIR spectra of **CP-1** and **rGO@CP-1** were recorded (KBr disk, 4000–400 cm^{-1}) on a Thermo Scientific NICOLET model (iS50). A UV-DRS (Lambda 35 spectrophotometer) instrument was used to record the maxima of **CP-1**. Thermal study (thermal gravimetric analysis) of **CP-1** and **rGO@CP-1** was performed on a TGA-50H instrument. To examine the bulk phase purity of **CP-1** and **rGO@CP-1**, powder X-ray diffraction patterns were recorded on a Brucker D8 Advance series 2 powder diffractometer (CuKa radiation scan rate 30/min, 293K). The scanning electron microscopy (SEM) (JEOL JSM-6510 model) coupled with JEOL/EO format was utilized to examine the morphology and particle heterostructure of **CP-1** and **rGO@CP-1**, respectively. The high-resolution transmission electron microscopy (HR-TEM) with EDS mapping and SAED analysis were

© 2024 The Author(s). Published by the Royal Society of Chemistry

Open Access Article. Published on 01 October 2024. Downloaded on 2/13/2026 7:18:18 AM.
This article is licensed under a Creative Commons Attribution-NonCommercial 3.0 Unported Licence.

performed on a TEM Thermo Scientific, Talos F200X G2 of **rGO@CP-1**. To examine the sensing properties of **CP-1**, fluorescence emission spectra of **CP-1** were performed using an Agilent Cary Eclipse Fluorescence spectrophotometer. The energy storage (electrochemical) properties on charging–discharging of **CP-1** and **rGO@CP-1** were determined at room temperature using three electrode systems (PGSTAT204 N, Metrohm Autolab, Netherlands).

2.3 Single crystal X-ray refinement

The crystallographic data of **CP-1** was collected by employing an 'XtaLAB Synergy, Rigaku, Japan' at a temperature of 293(2) K. The radiation used was monochromatic Mo-Kα radiation with a wavelength of 0.71073 Å. The International Tables for X-ray Crystallography were consulted in order to obtain the linear absorption coefficients and the anomalous dispersion corrections of the single-crystal structure.[48] Olex2 was used to determine the crystal structure, which was then solved with olex-2.solve[49] structure solution program by employing charge flipping. Finally, the olex2.refine refinement package was utilized to refine the structure by employing Gauss–Newton minimization technology. The anisotropic displacement parameter was used to refine all of the atoms that were not hydrogen.[50] Table S1 (ESI†) provides a summary of the data about the refinement of the crystal structure of **CP-1**, as well as other information regarding the bond lengths and bond angles of **CP-1** (Tables S2 and S3, ESI†).

2.4 Synthesis of CP-1

A solvothermal approach was utilized in order to accomplish the development of complex **CP-1**. 1,3-Di(4-pyridyl)propane (DPP) (50 mg, 0.25 mmol) was thoroughly mixed in 5 mL of methanol using a magnetic stirrer. Following this, two drops of aqueous sodium hydroxide (NaOH) (1 mol) were added in order to modify the slightly alkaline medium. Moreover, the copper nitrate (80 mg, 0.33 mmol) was solubilized in 5 mg of DI water. Furthermore, the copper nitrate solution was added dropwise in the DPP solution to homogenize the solution. Afterward, the resulting solution was transferred into a Teflon-lined stainless steel autoclave and kept at 100 °C for 48 h in a solvothermal oven. After completion of the reaction process, the reaction was cooled down to room temperature, and a clear solution was obtained that was kept for slow evaporation after filtration. After 1–2 weeks, blue colored needle-shaped crystals were obtained, which were suitable for SC-XRD data collection (Scheme 1). Yield 75%, melting point (218 °C), IR (cm^{-1}): 3464 (br), 3068 (m), 2934 (s), 2854 (m), 2467 (s), 1622 (s), 1557 (w), 1512 (w), 1382 (s), 1317 (s), 1233 (s), 1069 (s), 1023 (w), 859 (m), 817 (s), 523 (s), 452 (m).

2.4.1 Synthesis of reduced graphene oxide (rGO). The synthesis of **rGO** was conducted using Hummer's process with slight modifications.[51,52] The mixture of graphite powder and $NaNO_3$ (2 : 1) was slowly added to concentrated H_2SO_4 (150 mL) at a low temperature. In addition, the mixture was placed on a magnetic stirrer and maintained at a temperature range of 10–15 °C. Then, the solution of $KMnO_4$ was carefully added drop by drop to the resulting solution. The reaction temperature was kept at room temperature, and the reaction was stirred continuously for 20 hours. This led to the formation of a brownish viscous mixture. Distilled water (250 mL) was added to the mixture to dilute the solution and the temperature was allowed to fall below 50 °C. H_2O_2 (30%) (10 mL) was added into the resulting mixture solution, and the solution colour was changed into bright yellow colour with bubbles *i.e.*, indication of completion of the reaction. Again, the mixture was stirred for 4 h. After this the mixture was filtered and treated with 10% HCl solution, distilled water and then ethanol to get the pure product. The filtered product (GO) was dried out and 150 mg of this product was used to convert it into graphene oxide by dispersion followed by sonication for 1 h. To reduce this graphene oxide, a solution of $NaBH_4$ (1.5 g $NaBH_4$ into 9 mL distilled water) was added to the earlier formed graphene oxide dispersion. Additionally, the mixture was placed under reflux at a temperature of 100 °C and stirred continuously for 24 hours. Following this step, the mixture underwent filtration and the resulting product was thoroughly rinsed with distilled water and ethanol. After completing the necessary steps, the product was dried in a vacuum oven and its confirmation was obtained through PXRD. Yield 82%, IR (cm^{-1}): 3427 (br), 2922 (s), 2854 (m), 1717 (m), 1573 (m), 1461 (m), 1386 (w), 1221 (br), 1019 (m), 440 (w).

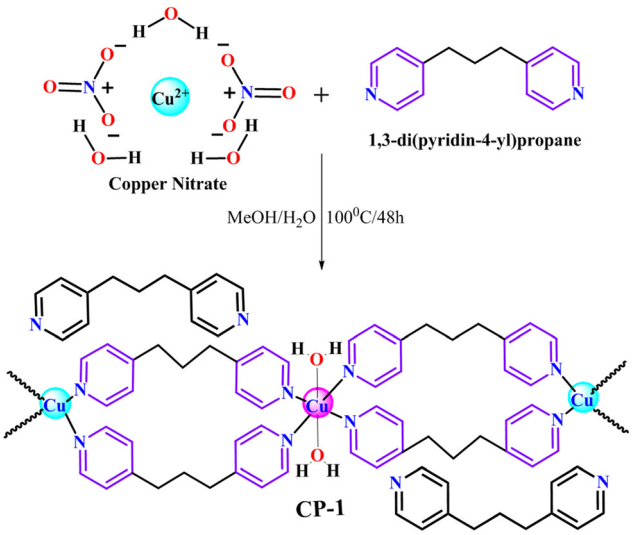

Scheme 1 Synthetic representation of **CP-1**.

2.4.2 Synthesis of rGO@CP-1. The fabrication of the **CP-1** composite (**rGO@CP-1**) was done by a mechanochemical grinding approach.[53,54] The composite was fabricated utilizing **CP-1** and the synthesized **rGO**[52] using (10 : 1) (w/w). The appropriate amounts of **CP-1** (500 mg) and **rGO** (50 mg) were added together in a ball milling agate jar (500 mL) and the grinding of the mixture was done under optimized conditions for 60 minutes at a rotational speed of 500 rpm; after that, the color of the mixed powder was changed.[44] Furthermore, 2 mL of ethanol was added to homogenize the mixture powder followed by a drying process in a vacuum oven. This process was repeated 2–3 times

Open Access Article. Published on 01 October 2024. Downloaded on 2/13/2026 7:18:18 AM.
This article is licensed under a Creative Commons Attribution-NonCommercial 3.0 Unported Licence.

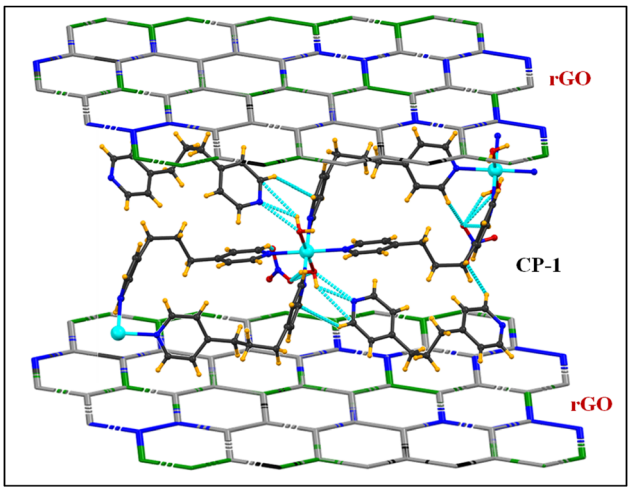

Scheme 2 Plausible schematic representation of the **rGO@CP-1** composite. Other atoms and functional groups are omitted for structural clarity.

to get the desired composite (Scheme 2). Then, the powdered form of the composite was characterized. IR (cm^{-1}): 3426 (br), 2919 (m), 2854 (w), 2427 (w), 1619 (s), 1389 (s), 1313 (m), 1227 (m), 1035 (s), 810 (m), 520 (m), 444 (m).

2.5. Fabrication of electrodes

The electrochemical evaluation of the **CP-1** and composite materials was performed using a three-electrode setup, with 1 M H_2SO_4 as the electrolyte. The Ag/AgCl electrode has been identified as the reference electrode, while a platinum wire serves as the counter electrode. A composite blend consisting of 80% **CP-1** and **rGO@CP-1** materials, 10% acetylene black, and 10% polytetrafluoroethylene was prepared for the fabrication of the working electrodes. The produced slurry was used to coat a piece of carbon fabric measuring 2 × 1 cm^2. After creating the electrodes, we conducted a thorough electrochemical analysis utilizing several techniques such as cyclic voltammetry (CV), galvanostatic charge–discharge (GCD), and electrochemical impedance spectroscopy (EIS). These measurements were performed using an Autolab potentiostat acquired from the Netherlands. The evaluations were performed at ambient temperature, extensively examining the electrochemical characteristics of the electrode materials manufactured in their original form.

3. Results and discussion

3.1 Structural description and topological analysis of CP-1

The crystal structure of **CP-1** was confirmed by utilizing single crystal X-ray diffraction (SCXRD) which reveals that the structure was crystallized in the triclinic crystal system with $P\bar{1}$ space group. The asymmetric unit of **CP-1** consists of two Cu(II) ions (both Cu1 and Cu2 have 0.5 crystallographic occupancies), three [1,3-di(4-pyridyl)propane] (DPP) ligands, in which two are coordinated with the copper(II) metal ion and the third is uncoordinated, and two nitrate ions in the lattice (Fig. 1a). Cu1 and Cu2 ions have a distorted octahedral geometry surrounded by four nitrogen atoms of the DPP linker and two oxygen atoms of coordinated water molecules (Fig. 1c). The extended connectivity represents a one-dimensional staircase-like polymer network. Hydrogen bonding and C–H···π interactions led to a three-dimensional supramolecular network (Fig. 1b). The topological analysis was examined with the help of ToposPro software.[55,56] The standard rod net representation of **CP-1** shows a ***1,3M4-1*** underlying net for the two fragments. Furthermore, the simplified TTD collection of the hydrogen

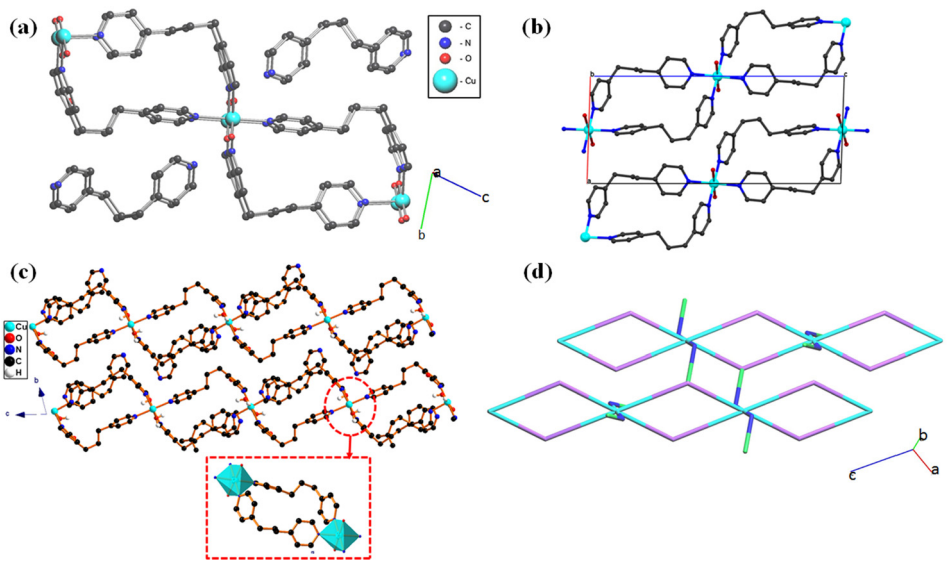

Fig. 1 (a) Molecular representation of **CP-1** along the crystallographic bc plane, (b) molecular packing structure with a staircase pattern, (c) supramolecular structure with a polyhedron view, and (d) topological view of **CP-1** with ***2C1*** topology. (Nitrate ions and hydrogen atoms are omitted for structural clarity.)

© 2024 The Author(s). Published by the Royal Society of Chemistry

Open Access Article. Published on 01 October 2024. Downloaded on 2/13/2026 7:18:18 AM. This article is licensed under a Creative Commons Attribution-NonCommercial 3.0 Unported Licence.

bonded network of **CP-1** represents the point symbol (PS) {0}; 2-c nimodal net with ***2C1*** topology (Fig. 1d).

3.2 FT-IR, PXRD, SEM, HR-TEM and TGA analysis

The crystal structure of **CP-1** was determined by the single crystal X-ray technique. Moreover, chemical and physical behaviors such as phase purity, functionality, particle morphology, and thermal stability of the synthesized **CP-1** and **rGO@CP-1** were established by PXRD, FTIR, SEM, and TGA techniques. The UV-DRS spectrum of **CP-1** showed maximum absorbance at 295 nm corresponding to $\pi \rightarrow \pi^*$ transition (Fig. S1, ESI†). The FT-IR studies show vibrational bands of different intensities due to Cu–O, Cu–N, C═C, C–H, and C═N bonds. The Fourier transform infrared (FTIR) spectra of the **CP-1** and **rGO@CP-1** composite showed a broad band at 3464 and 3426 cm^{-1} that could be attributed to the presence of hydroxide (–OH) functional groups. Asymmetric and symmetric vibration bands of **CP-1** and **rGO@CP-1** at 1622, 1619 cm^{-1} and 1382 cm^{-1}, 1389 cm^{-1} could be assigned to the presence of υ_{asy} COO^- and υ_{sy} COO^- functional groups, respectively.[41] The vibrational absorption bands at 523 and 520 cm^{-1} could be due to the presence of the Cu–O bond. Vibration frequencies at 452 and 444 cm^{-1} can be attributed to the Cu–N bond.[41,57] Similarly, the vibrational frequency of **rGO** at 3435 cm^{-1} is due to the presence of –OH functional groups. A strong band appeared at 1725 cm^{-1} corresponding to the C═O functional group. Other vibrational frequencies at 606, 503, and 420 cm^{-1} could be attributed to the presence of triclinic phase formation of **rGO** (Fig. S2, ESI†). To identify the structural integrity in the bulk phase of **CP1**, the powder X-ray diffraction (PXRD) pattern was performed, which was well matched with the simulated pattern of **CP-1** (Fig. S3a, ESI†). Similarly, the PXRD pattern of **rGO** was well matched at 24.10° (002) and 43.41° (100) that is situated within range.[58] The **rGO** peaks at 2θ (24.10°) suggested that **rGO** is obtained in fully reduced form with a 3.5 Å interlayer distance, which indicates that the polyhydrocarbon template is not present.[59] Moreover, shifting of particular peaks at 24.68° and 43.77° in **rGO@CP-1** indicated that the addition of **rGO** over **CP-1** was done successfully with the stacking layer pattern (Fig. S3b, ESI†). Thermal stability of **CP-1** was examined by using TGA analysis under a N_2 atmosphere at the rate of 10 °C min^{-1}. The TGA curve reveals an initial weight loss (~4.5%) of **CP-1** up to 100–165 °C due to elimination of lattice and coordinated water molecules. Another weight loss (calcd. 38.6%) occurs up to 290 °C corresponding to the elimination of the DPP organic ligand of the lattice. Furthermore, weight loss occurs due to the elimination of nitrate molecules up to ~500 °C and after that the framework collapses. Similarly, the thermal analysis of **rGO@CP-1** follows the same decomposition pattern as that of **CP-1** (Fig. S4, ESI†). This could be attributed to weak interactions between **CP-1** and the **rGO** functionality. The surface morphology of **CP-1** and **rGO@CP-1** was analyzed by SEM analysis at different magnification ranges. The SEM analysis of **CP-1** showed flakes with a disoriented structural morphology at different magnification ranges (Fig. 2a–c). The flaky type morphology could provide more reactive sites with more reaction compatibility for better electrochemical reaction.[41] Similarly, SEM analysis of **rGO@CP-1** showed adhesive clump formation of reduced graphene oxide at the surface of **CP-1** due to weak interaction between them. As per the morphology of **rGO@CP-1**, **rGO** successfully interacted over the **CP-1** particles (Fig. 2d–f). The structural morphology of **rGO** showed a sheet-like structure at different magnification ranges (Fig. S5a, ESI†). Furthermore, the compositions of **CP-1** (Fig. 3) and **rGO@CP-1** (Fig. S5b, ESI†) were authenticated by elemental mapping of particular elements in the 1 mm range. The mapping of **rGO@CP-1** showed a slightly high composition of carbon and oxygen that could be an indication of successive composite formation. In the fabrication of **rGO@CP-1**, weak interactions could play the main role.[44] Moreover, the

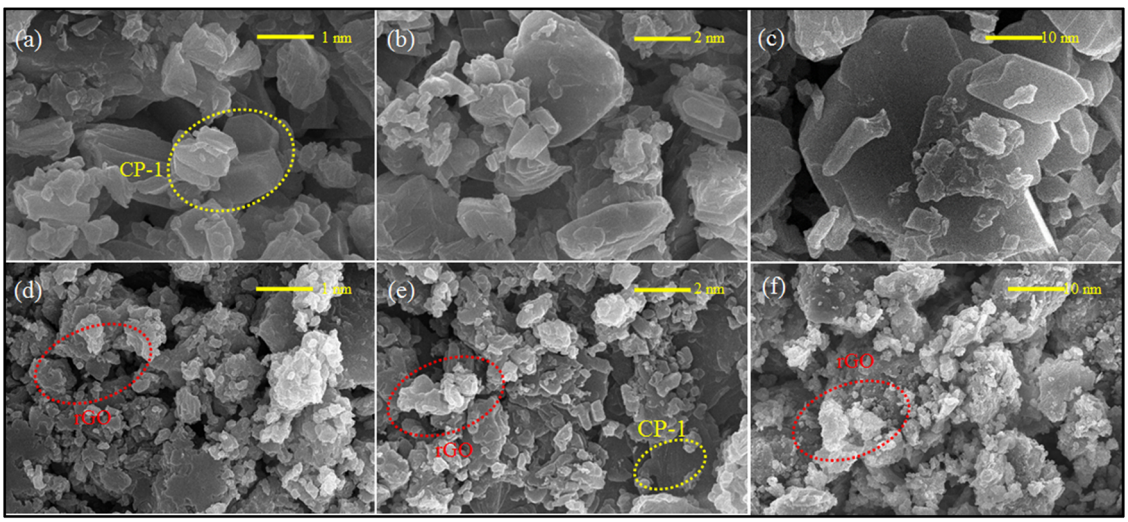

Fig. 2 SEM images of the prepared **CP-1** showing the particle morphology at different magnification ranges (a)–(c), images of the **rGO@CP-1** composite represent the adhering of **rGO** on **CP-1** at different magnification ranges (d) and (e), and surface morphological behavior of **CP-1** and **rGO@CP-1** were executed within the 1–10 nm scale range. (yellow circles represent **CP-1** particles and red circles for **rGO**).

Open Access Article. Published on 01 October 2024. Downloaded on 2/13/2026 7:18:18 AM.
This article is licensed under a Creative Commons Attribution-NonCommercial 3.0 Unported Licence.

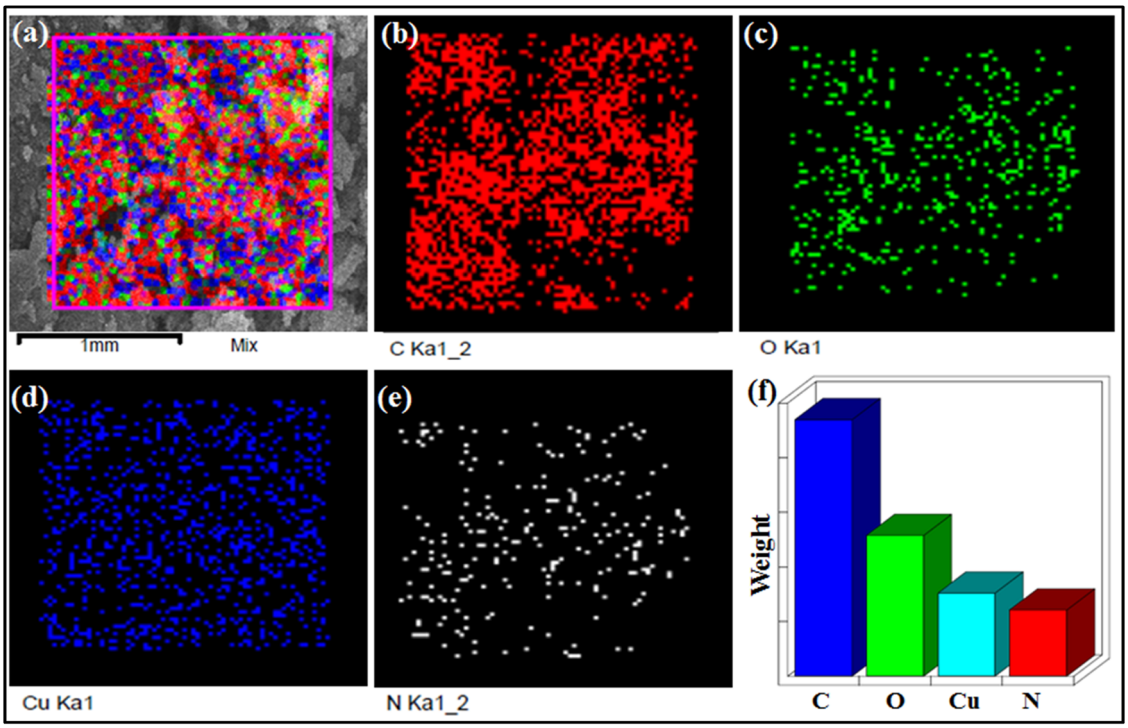

Fig. 3 Elemental mapping of **CP-1** was recorded at 1 mm mixed selective area (a)–(f).

fabrication of **rGO@CP-1** was also confirmed by HR-TEM analysis with EDX, which indicated the uniform deposition of **CP-1** on the surface of **rGO** (Fig. 4). The loaded particles of **CP-1** showed an irregular circular shape with a good particle size of 15–25 nm. The single particle image clearly showed the lattice fringes that were devoted to the presence of copper metal with a lattice spacing of about 0.33 nm (Fig. S5c, ESI†).[60]

3.3. Luminescence sensing

A finely ground sample of **CP-1** weighing 3 mg was placed in 4 mL of various solvents for luminescence measurements. The mixture underwent ultrasonication for 25 minutes and was allowed to age for 24 hours, resulting in the formation of stable suspensions. The suspensions were analyzed for their emission spectra at room temperature, covering a wavelength range of 200–600 nm. The measurements were conducted with illumination at 300 nm. The luminescence intensities of the **CP-1** suspension varied depending on the solvent molecules used. The emission intensity of EtOH of **CP-1** was significantly high at 360 nm when excited at 300 nm. The luminescence experiments were conducted in EtOH solution of various metal ions using **CP-1**. **CP-1** (3 mg) was placed in 4 mL of various metal cations $M(NO_3)x$, in EtOH with a concentration of 5×10^{-4} M (M = Co^{2+}, Cd^{2+}, Zn^{2+}, Fe^{3+}). In addition, the mixed solutions underwent ultrasonication for 25 minutes before being used for luminescence recognition measurements. Eqn (1) is used to calculate the luminescence quenching efficiency (Q).[61]

$$Q(\%) = \{(I_0 - I)/I_0\} \times 100 \quad (1)$$

The luminescence emission intensities prior to and following the addition of solvents or metal ions are denoted by the symbols I_0 and I, respectively.

3.3.1 Detection of analytes. To efficiently assess the potential of **CP-1** to display a luminescent reaction to different chemical substances. It is fascinating how the luminescence spectrum in **CP-1** is greatly influenced by the solvent molecules, particularly DMF, which exhibits the most potent quenching properties. DMF transmittance at 300 nm is about 97%, and this absorption by DMF may cause an effect of inner filter that decreases the resulting emission. The luminescent intensity of **CP-1** for different solvents is shown in Fig. 5a. The quenching efficiencies for different solvents were calculated to be 0.0% (ETOH), 65.8% (DMSO), 72.0%, 85.0% (H_2O), 85.0% (TEA), 97.4% (DMF) (Fig. 5b). DMF exhibited the most significant quenching response. To assess the sensing sensitivity of DMF, a quantitative fluorescence titration experiment was conducted. Drop-by-drop additions of DMF solutions were made to a stable **CP-1** dispersion solution. After stabilization, the fluorescence intensity was measured independently. When the DMF concentration was gradually increased, there was a noticeable decrease in fluorescence intensity, as shown in Fig. 6a. In addition, the quenching constant was determined using the Stern–Volmer (S–V) equation: $I_0/I = 1 + K_{sv}[M]$.[62] The experimental data shows a strong linear correlation coefficient (R^2 = 0.9987) for DMF. Additionally, the calculated result of K_{sv} at low concentration is 6.41×10^4 M^{-1} for DMF (Fig. 6b). The minimum detection limit is 12.34×10^{-6} M (0.91 ppm) and it was calculated using the formula LOD = $3\sigma/m$, where σ represents the standard error and m represents the slope.

© 2024 The Author(s). Published by the Royal Society of Chemistry

Open Access Article. Published on 01 October 2024. Downloaded on 2/13/2026 7:18:18 AM.
This article is licensed under a Creative Commons Attribution-NonCommercial 3.0 Unported Licence.

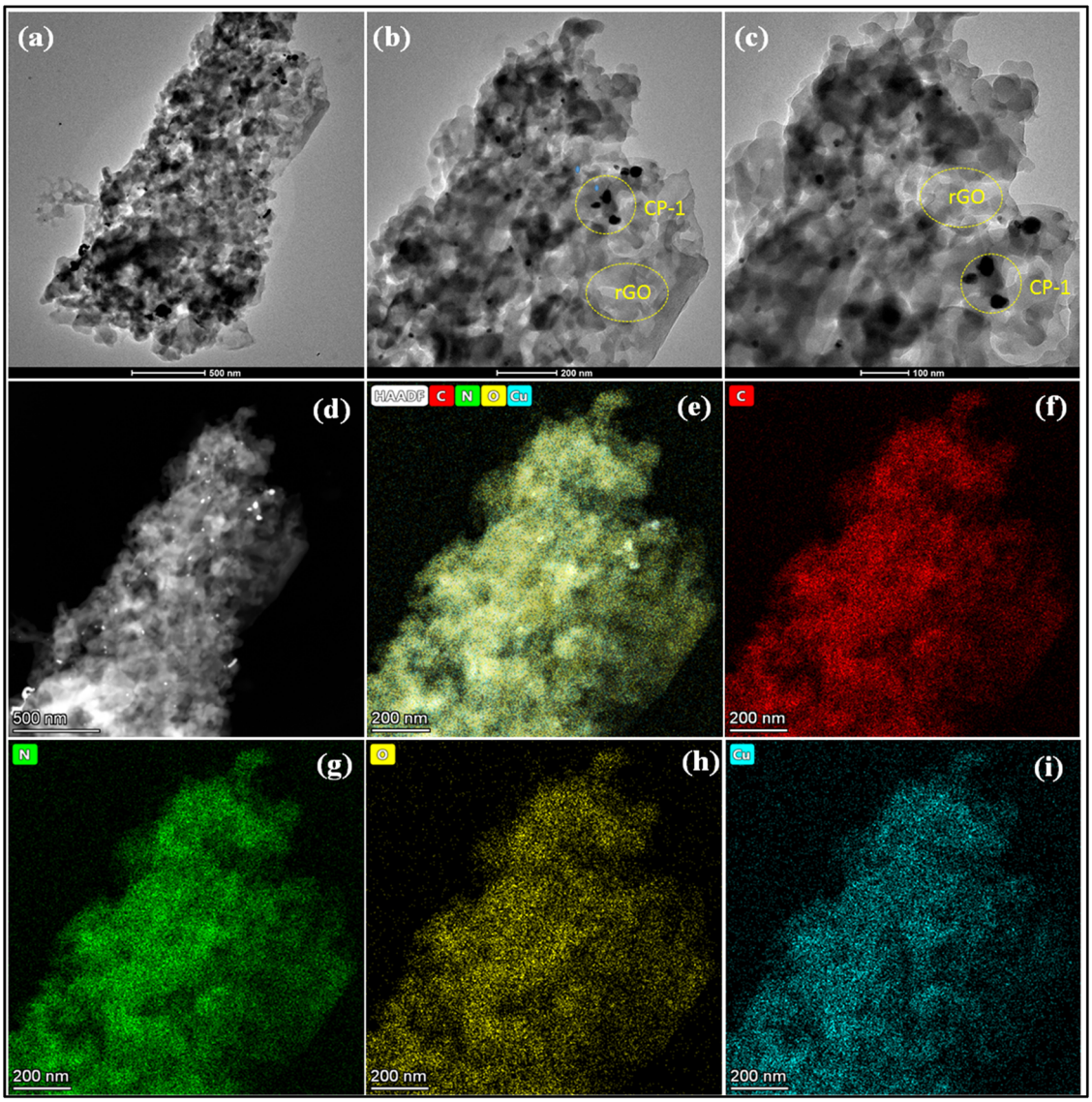

Fig. 4 HR-TEM image of **rGO@CP-1** at different magnification ranges (a)–(c), HAADF image of the selected area at 500 nm magnification range (d), and elemental mapping of **rGO@CP-1** (e)–(i).

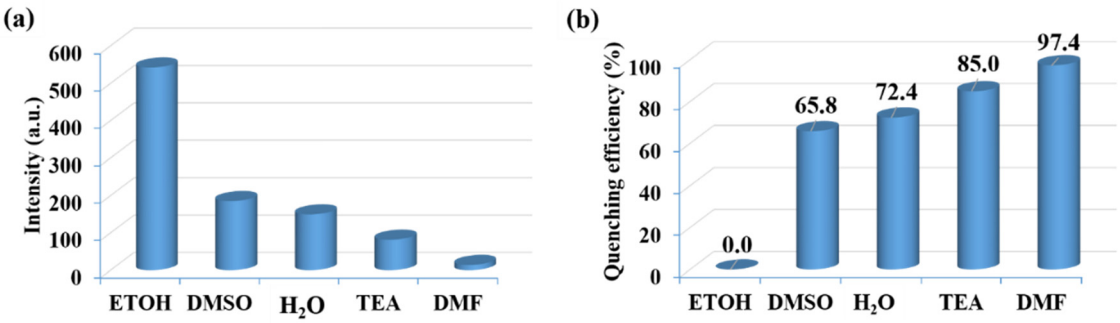

Fig. 5 (a) Luminescence emission intensities and (b) luminescence quenching efficiencies for **CP-1** in the presence of different organic solvents.

To investigate the luminescent reactions of **CP-1** with various metal cations, the **CP-1** was immersed in EtOH solution containing the same concentration (5×10^{-4} M) of different metal cations. After 24 hours, the resulting luminescent spectra

Open Access Article. Published on 01 October 2024. Downloaded on 2/13/2026 7:18:18 AM.
This article is licensed under a Creative Commons Attribution-NonCommercial 3.0 Unported Licence.

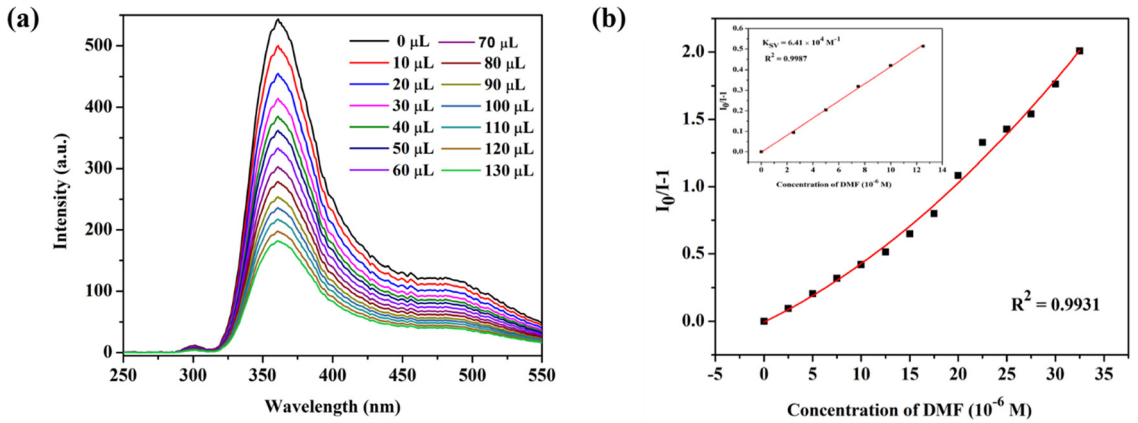

Fig. 6 (a) Fluorescence emission intensities when an amount of DMF is added dropwise to the EtOH solution of **CP-1**, and (b) the S–V plot of **CP-1** dispersed in EtOH solution after dropwise additions of DMF (1 mM) and the linear S–V curve of **CP-1** at low concentration of DMF (inset).

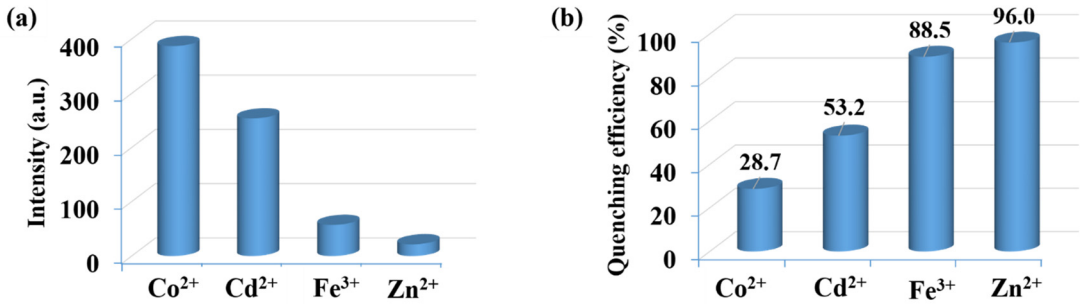

Fig. 7 (a) Luminescence emission intensities and (b) luminescence quenching efficiencies of **CP-1** dispersed in different metal ion EtOH solutions (5×10^{-4} M) at 360 nm.

were recorded. Fig. 7a displays the relative luminescence intensities of **CP-1**. The efficiency of relative luminescence quenching for metal ions was observed as follows: 28.7% for Co^{2+}, 53.2% for Cd^{2+}, 88.5% for Fe^{3+}, and 96.8% for Zn^{2+}, as shown in Fig. 7b. To find out the limit of detection (LOD) of Zn^{2+} in EtOH medium, a quantitative fluorescence titration experiment was conducted. Drop by drop additions of aqueous solutions (1 mM) of Zn^{2+} were made to a stable **CP-1** dispersion solution. After stabilization, the fluorescence intensity was measured independently. When the Zn^{2+} concentration was increased, there was a noticeable decrease in fluorescence intensity (Fig. 8a). The experimental data shows a high linear correlation coefficient (R^2 = 0.9952) for Zn^{2+}. Additionally, the calculated result of K_{sv} at low concentration is 4.89×10^4 M^{-1} for Zn^{2+}

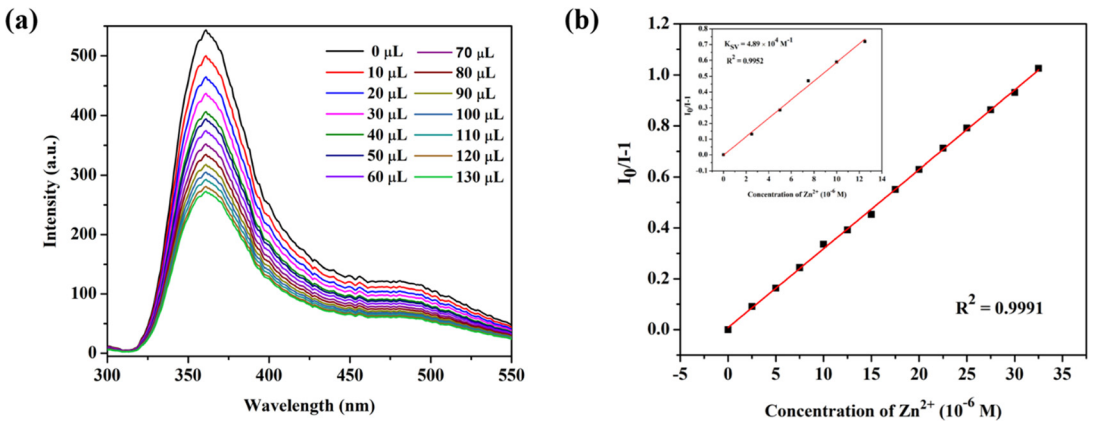

Fig. 8 (a) Fluorescence emission intensities when an amount of Zn^{2+} is added dropwise to the EtOH solution of **CP-1** and (b) the S–V plot of **CP-1** dispersed in EtOH solution after dropwise additions of Zn^{2+} (1 mM) and the linear S–V curve of **CP-1** at low concentration of Zn^{2+} (inset).

© 2024 The Author(s). Published by the Royal Society of Chemistry

Open Access Article. Published on 01 October 2024. Downloaded on 2/13/2026 7:18:18 AM.
This article is licensed under a Creative Commons Attribution-NonCommercial 3.0 Unported Licence.

(Fig. 8b). The minimum detection limit is 5.31×10^{-6} (0.171 ppm) at 360 nm wavelength.

3.3.2 Recyclability and reusability. The practical utility of the luminous sensor is enhanced by its ability to serve as a sensing material in various applications. Consequently, an inquiry was carried out to assess the recycling efficiency of **CP-1** as a fluorescent indicator for detecting DMF and Zn^{2+} in EtOH-based solution. After the sensing experiment was finished, the mixture that had been spread in the DMF and Zn^{2+} EtOH-based solution was collected. Several water centrifugations were conducted on the sample to eliminate any residual DMF and Zn^{2+} present on the surface. After the sensing procedure, the emission intensity remained constant, with fluctuations according to the photoluminescence spectrum. After five cycles, there was a modest decrease in the intensity of the luminescence, possibly caused by the transfer of energy and the lingering presence of ions on the surface. However, the quenching performance remained consistent for all ions even after completing a series of cycles (Fig. 9).

3.3.3 Sensing mechanism. Previous studies have suggested that the recognition of metal cations and solvents is often influenced by framework collapse, ion exchange between various analytes, and competitive absorption/interaction, and these processes are also commonly implicated.[63] Additional tests were performed to gain a better understanding of how **CP-1** senses Zn^{2+} and DMF through quenching impacts. In order to examine the inhibition mechanism caused by Zn^{2+} and DMF, we conducted measurements using UV-vis spectra. The collapse of the **CP-1** complex is not responsible for the quenching of fluorescence.[64,65] The decrease in fluorescence intensity observed during the electron-transfer transitions of the Zn^{2+} and DMF can be attributed to the diminishing energy transfer occurring between the π and π* orbitals of the ligands containing nitrogen. We utilize an excitation wavelength of 300 nm to record the sensing data. This specific wavelength is chosen because it corresponds to the excitation peak of the fluorophore, ensuring maximum absorption and efficient excitation. By using 300 nm, we achieve optimal fluorescence emission, which enhances the sensitivity and accuracy of the experiment. This choice also minimizes background interference, thereby providing more reliable and precise results under the experimental conditions. The likelihood of resonance energy transfer is determined by the degree of spectral overlap between the excitation bands of the fluorescence detectors **CP-1** and the absorption bands of the metal ions (analytes). Fig. S6 (ESI†) clearly shows that there is a significant overlap between the excitation and absorption spectra of **CP-1** and Zn^{2+} and DMF. The mechanism was consistent with those presented by other groups.[66,67] Among all metal ions and solvents, Zn^{2+} and DMF have a higher tendency to quench due to their UV-vis absorption spectra, which significantly overlap with the excitation spectra of **CP-1**. The conclusion can be drawn from these factors that the overlaps between the **CP-1** and Zn^{2+} and DMF UV-vis spectra suggest that the metal ions and solvents are in competition with organic ligands for the absorption of excitation wavelength energy. This competition leads to the quenching effect.[68,69]

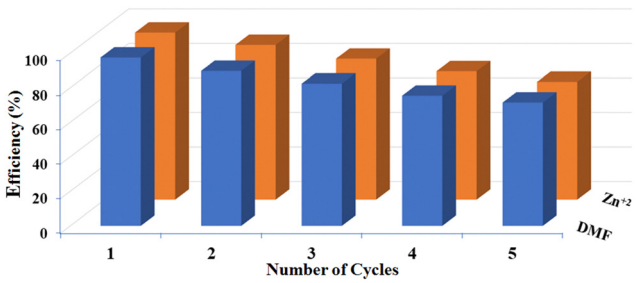

Fig. 9 Quenching efficiency of DMF and Zn^{2+} over **CP-1** at 360 nm.

3.3.4 Electrochemical studies. The electrochemical characteristics of the prepared working electrodes, specifically **CP-1** and composite, were examined utilizing CV at various scan rates ranging from 10 to 300 mV s^{-1}. These evaluations were performed within a potential window (0–1.0 V) in a 1 M electrolyte solution of H_2SO_4, as depicted in Fig. 10. The CV profiles reveal distinctive features of the working electrodes. **CP-1** exhibits a discernible couple of redox peaks, indicating its electrochemical behavior. Conversely, the CV spectrum of **CP-1** aligns with the electric double-layer capacitance mechanism, manifesting nearly rectangular characteristics that suggest efficient charge propagation on the surface of the carbon cloth. Notably, **rGO@CP-1** demonstrates a significantly enhanced current response and charge transfer, which is evident in the increased integrated area. This improvement is due to synergistic effects caused by the combination of pseudo-capacitive **CP-1** and **rGO@CP-1** electric double-layer (EDL) capacitive characteristics.

Fig. 10a illustrates the CV plots of the prepared working electrodes across various scan rates ranging from 10–300 mV s^{-1}. Notably, the region beneath each curve of the CV expands as the scan rates increase across both electrodes. Remarkably, the incorporated area of the composite electrode exceeds that of the other electrode, showing a considerable increase in specific capacitance due to the synergistic interaction of **CP-1** crystals and **rGO** sheets. The CV profile of **rGO@CP-1** reveals distinct redox peaks attributed to the pseudo-capacitive behaviour of **CP-1** (Fig. 10b). However, the electrode tends to adopt a semi-rectangular form at higher scan rates, indicating that electrolyte ions are diffusing more quickly. This phenomenon likely contributes to an increased charge storage capacity, as depicted in Fig. 10b. The structure of **CP-1** increases the area of contact and modes in the system, allowing for more efficient charge transfer.[53,54,70] However, the inherent low conductivity of **CP-1** limits its application in electrochemical contexts. Hence, the introduction of **rGO** alongside **CP-1** enhances the hybrid's conductivity. The wavy surface of **rGO**, with wrinkles preventing restacking, substantially improves conductivity by shortening the ion diffusion paths, thereby enhancing the electrochemical response.[71] The comparison of the CV profiles at 100 mV s^{-1} scan rate demonstrates the beneficial synergistic interaction between **rGO** sheets and **CP-1**. This synergy facilitates efficient charge

Open Access Article. Published on 01 October 2024. Downloaded on 2/13/2026 7:18:18 AM.
This article is licensed under a Creative Commons Attribution-NonCommercial 3.0 Unported Licence.

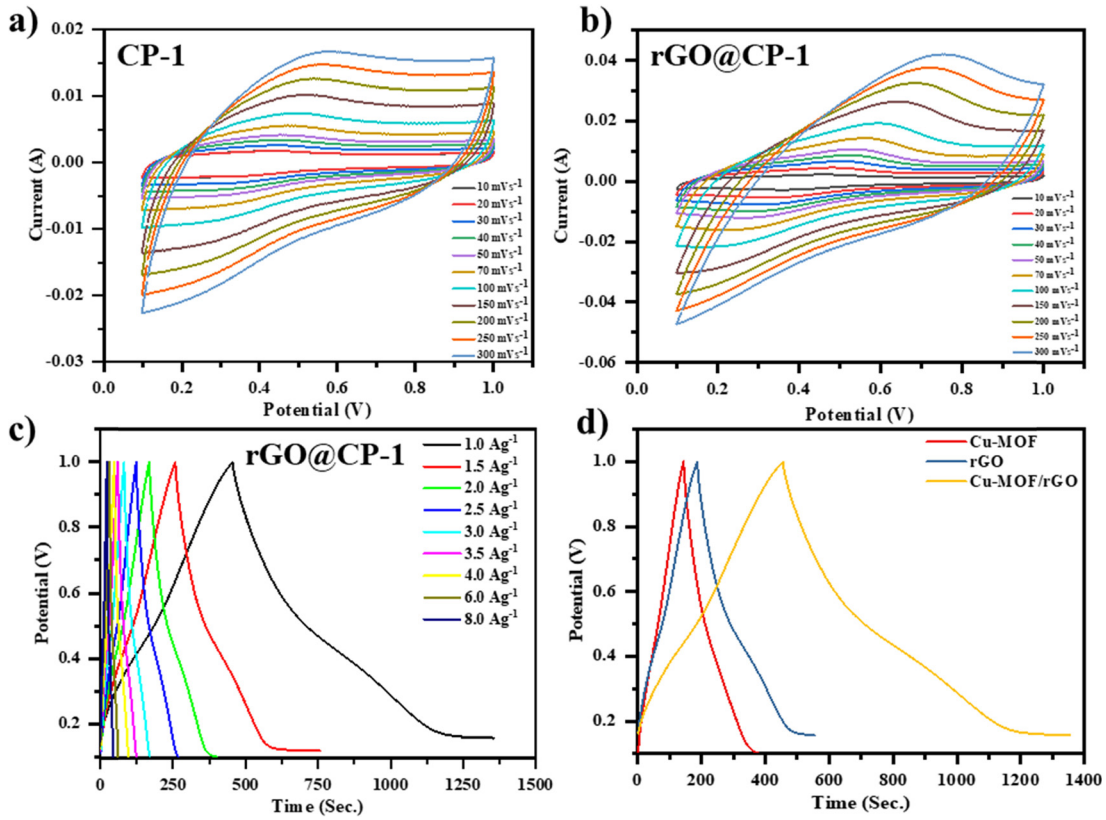

Fig. 10 (a) and (b) CV curve profile of **CP-1** and the composite (**rGO@CP-1**), and (c) GCD profile of te composite (**rGO@CP-1**) at different current densities, and (d) comparative GCD profile of **CP-1**, **rGO**, and the composite material at a current density of 1.0 A g^{-1}.

transfer, leading to an augmented integrated area and confirming the collaborative impact of both **rGO** sheets and **CP-1**.

GCD analysis was performed within a potential window of 0–1.0 V at current densities ranging from 1 to 8 A g^{-1} to evaluate the capacitive behavior of the fabricated electrodes (**rGO**, **CP-1**, and **rGO@CP-1**) in a 1 M H_2SO_4 aqueous electrolyte solution, as shown in Fig. S7(a and b) (ESI†) and Fig. 10c. The comparison of the charging–discharging profiles for prepared electrodes is depicted in Fig. 10d. **rGO@CP-1** exhibits a good discharging time, which indicates a better specific capacitance than the earlier reported electrode materials used in supercapacitor applications. The discharging time decreases with increasing current density and reducing the capacitance. Specifically, at a current density of 1 A g^{-1}, **CP-1**, **rGO**, and **rGO@CP-1** demonstrate specific capacitance values of 244.17 F g^{-1}, 408.07 F g^{-1} and 899.54 F g^{-1}.[72] The as-synthesized composite electrode material delivers remarkably high specific capacitance due to the synergistic effect among **rGO** and **CP-1**, and a comparative study was done (Table 1).

Furthermore, the efficiency of the electrodes is assessed by graphing specific capacitance *vs.* current density (Fig. 11a), which reveals a reduction in charge storage ability with increasing current density due to insufficient occupancy of active ionic species. The stability of the composite material (**rGO@CP-1**) was evaluated through $\left(C_s = \frac{I \times \Delta t}{m \times \Delta V}\right)$ and Coulombic

Table 1 Comparative study of various reported Cu(II)-based CPs and their composites

S. no.	MOF	Electrolyte	Current density (A g^{-1})	Capacitance (F g^{-1})	Ref.
1.	Cu-MOF@ACNF	1 M H_2SO_4	1.0	303.2	73
2.	$[Cu_3(Azopy)_3(BTTC)_3(H_2O)_3{\cdot}2H_2O]_n$	1 M Na_2SO_4	0.8	244.2	74
3.	Cu-MOF-1	6 M KOH	1.0	181	75
	Cu-MOF-2			248	
4.	Cu-MOF based APC	6 M KOH	0.5	260.5	76
5.	Cu-MOF@**rGO** (*HMRL-1/R*)	1 M Na_2SO4	1.0	366.6	77
6.	Cu-DBC	1 M NaCl	0.2	479	78
7.	CuMOF/**rGO**	1 M Na_2SO_4	0.8	462	44
8.	CuO@**CP-1**	1 M H_2SO_4	1.0	602.25	54
9.	Cu(II) **CP-1**	1 M H_2SO_4	1.0	244.17	This work
	CP-1@rGO			899.54	

© 2024 The Author(s). Published by the Royal Society of Chemistry

Open Access Article. Published on 01 October 2024. Downloaded on 2/13/2026 7:18:18 AM.
This article is licensed under a Creative Commons Attribution-NonCommercial 3.0 Unported Licence.

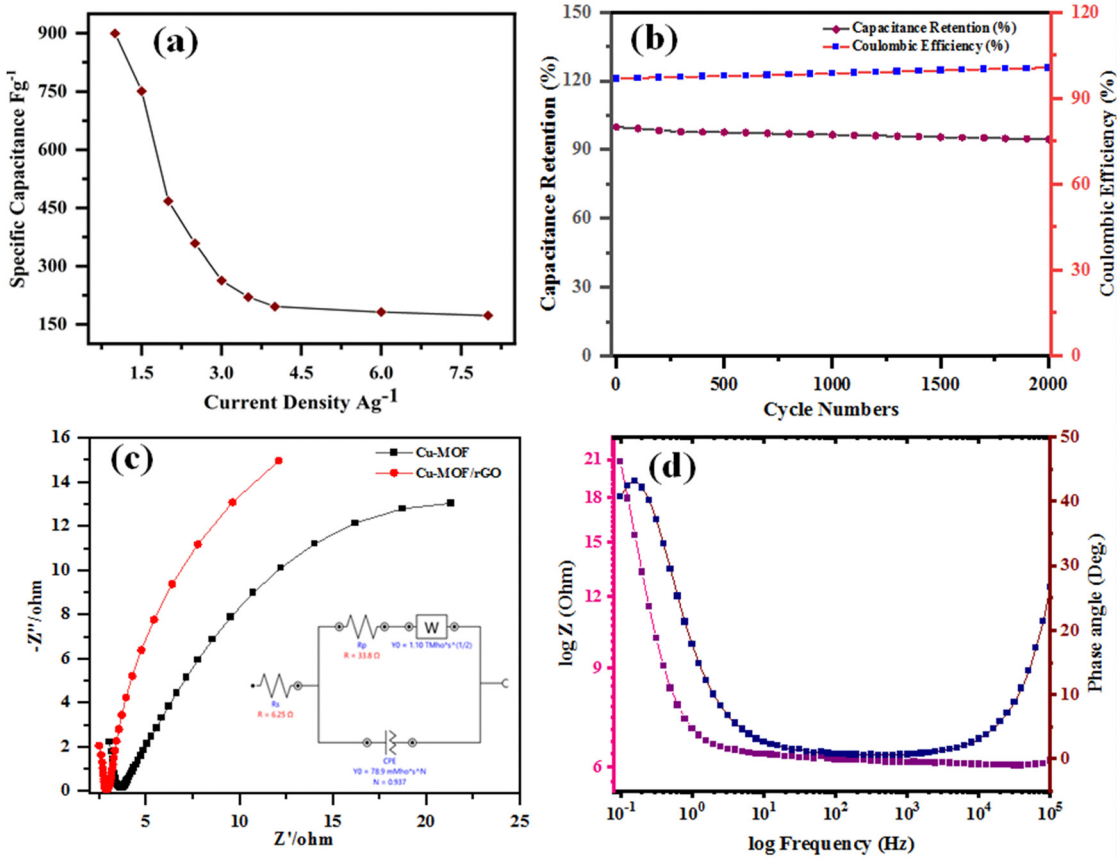

Fig. 11 (a) Specific capacitance *vs.* current density for the composite electrode, (b) cycling stability profile of **CP-1** and the composite electrode up to 2000 cycles at a current density of 8.0 A g^{-1}, (c) Nyquist plots of **CP-1** and **rGO@CP-1** electrode materials with the inset showing the equivalent circuit of the composite, and (d) Bode plot of **rGO@CP-1** electrode.

efficiency (CE), which was determined using the formula $\left(\eta = \frac{t_D}{t_C} \times 100\%\right)$ and was reported to be 98.6% with a capacity retention of 94.62% after 2000 charge–discharge cycles at 8.0 A g^{-1} current density, as shown in Fig. 11b.[52,79,80] This performance is attributable to the efficient facilitation of electrolyte ion transport inside the open-linked structure **rGO@CP-1** during rapid charging–discharging processes. Additionally, the resilient design of the **rGO@CP-1** spread on the outer surface of carbon cloth, induced synergistically, contributes to this outstanding outcome.

However, the rapid delivery of electrons and ions in the **rGO@CP-1** electrode can be attributed to its lower series resistance (R_s, encompassing solution resistance, contact resistance, *etc.*) and charge-transfer resistance (R_{ct}). Electrical resistance is a crucial parameter for evaluating SC electrodes, quantitatively determined by EIS over a frequency range of 100 kHz to 0.01 Hz at 10 mV potential amplitude, as depicted in Fig. 11c. Generally, the Nyquist plots for **CP-1** and **rGO@CP-1** electrodes exhibit similar patterns, consisting of a slight semicircle in the high-frequency region and a straight line in the low-frequency region, indicating diffusion control.[81] By using Nova software for calculation and modulation, the EIS data were accurately fitted to an equivalent circuit, shown in the inset of Fig. 11c. The R_s values for **CP-1** and **rGO@CP-1**, calculated from the points where the curves intersect the Z' axis (real axis), were 1.97 Ω and 6.25 Ω, respectively. Furthermore, the R_{ct} values determined and simulated using Nova software were approximately 5.93 Ω and 33.8 Ω. These results confirm that a lower concentration and extended soaking period are optimal conditions for synthesizing composite electrodes. Notably, the **rGO@CP-1** composite displays a lower R_s value as compared to **CP-1**. Significantly, the fabricated composite material exhibits a small R_{ct} compared to the **CP-1** material, indicating minimal R_{ct} at the electrolyte/electrode interface, attributed to the porous structure of the composite material.

In addition, the Bode plots of phase angle *versus* frequency and total impedance *versus* frequency are shown in Fig. 11d. Among the as-prepared electrode materials, the **rGO@CP-1** exhibited the highest phase angle of 40° in the low-frequency region, indicating a higher degree of pseudocapacitive behavior, which aligns with the results from CV and GCD measurements. This higher phase angle suggests more efficient electrolyte ion transport, producing the highest pseudocapacitive response. The plot of real impedance *versus* frequency shows different slopes across various frequency regions. All synthesized electrode materials exhibited an almost zero slope

Open Access Article. Published on 01 October 2024. Downloaded on 2/13/2026 7:18:18 AM.
This article is licensed under a Creative Commons Attribution-NonCommercial 3.0 Unported Licence.

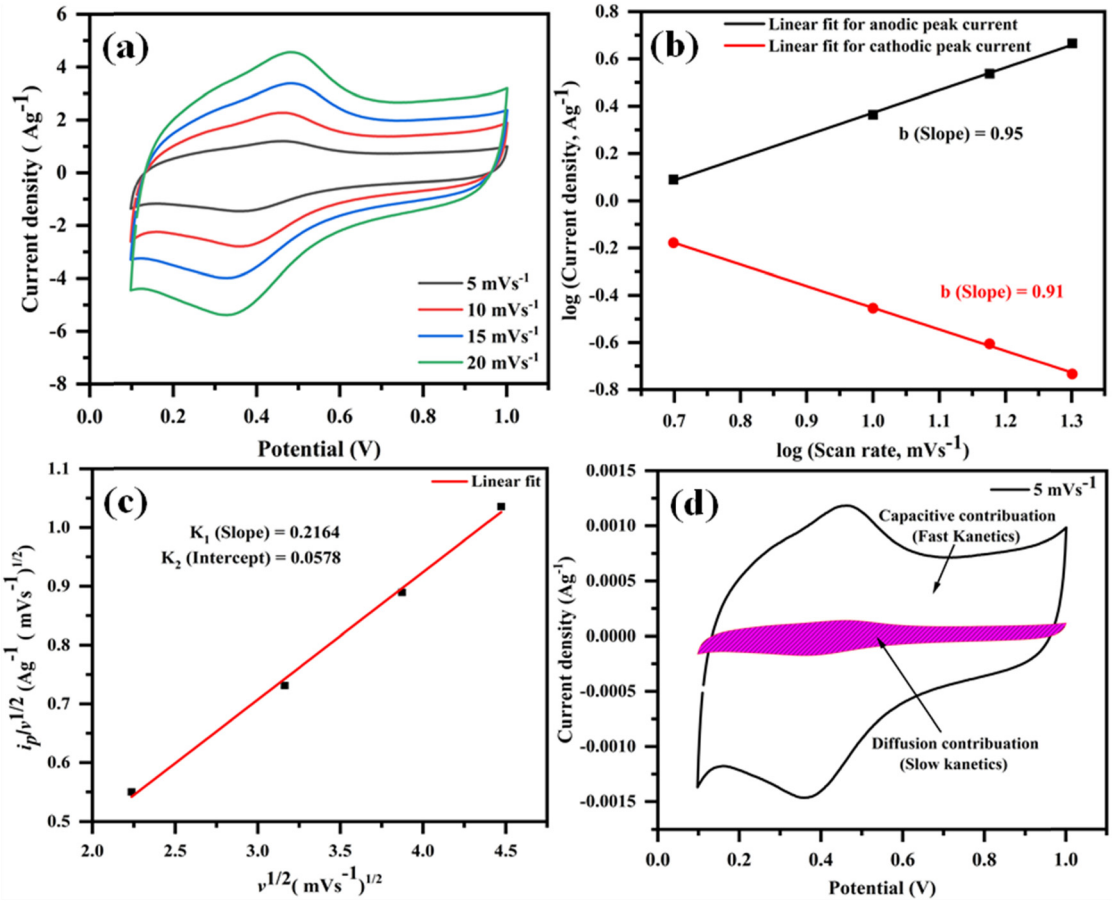

Fig. 12 The anodic and cathodic peaks at low scan rates as illustrated by CV plots (5–20 mV s^{-1}) (a); plot of $\log i_p$ *vs.* $\log v$ for (b); the peak current $(i_p)/(\text{scan rate})^{\frac{1}{2}}(v)^{\frac{1}{2}}$ *vs.* $(v)^{\frac{1}{2}}$ plot (c); plot of capacitive contribution to the total current in CV curve of **rGO**/Cu-(II) at 5 mV s^{-1} (d).

at high frequencies, indicating that the resistance at the electrode–electrolyte interface is dominant. In the low-frequency region, the electrodes displayed a purely capacitive nature without any resistance, suggesting that this composite electrode has both capacitive and resistive features.

Consequently, the capacitive behaviour is suppressed at high frequencies, and the resistive component becomes dominant, resulting in a phase angle of 26°. This study demonstrates that the **rGO@CP-1** electrode is promising for supercapacitors. The CV, GCD, and EIS characterization studies of the **rGO@CP-1** composite reveal that this electrode material possesses good capacitive behavior.

Moreover, to delve further into the energy storage mechanism of the optimized electrode material (**rGO@CP-1**), we analyzed the CV curves obtained at various scan rates in 1 M H_2SO_4 (Fig. 12a). Using the power law equation, we aimed to distinguish between diffusion-controlled faradaic redox (pseudocapacitance) and capacitive (EDLC) processes.[82]

$$i_p = av^b \text{ or } \quad \log i_p = \log a + b \log v$$

In this equation, "i_p" represents the peak current, and "ν" corresponds to the scan rate. By plotting $\log i_p$ against $\log \nu$, we obtain the slope (b) and intercept ($\log a$) values (Fig. 12b). These values offer crucial insights into the charge storage mechanism. Specifically, the slope (b) equals 0.5, indicating that the diffusion-controlled faradaic process predominantly governs the charge storage. Alternatively, if the value of b is 1, it suggests that the capacitive process dominates the reaction. However, when b falls between 0.5 and 1, diffusion-controlled and capacitive (EDLC) processes contribute to the overall storage mechanism.[83,84] Analysis of the plot of $\log i_p$ *versus* $\log \nu$, recorded for the anodic and cathodic peaks at 0.48 V and 0.36 V, reveals b values of 0.95 and 0.91, respectively (Fig. 12b). This observation indicates that the charge storage mechanism involves diffusive and EDLC processes. Moreover, an analysis of diffusive and capacitive behavior is conducted using the Dunn equation: $i_p = k^1\nu + k^2\nu^{1/2}$, where i_p denotes the current at a particular voltage, and $k^1\nu$ and $k^2\nu^{1/2}$ signify the capacitive and diffusive contributions, respectively. Using this equation, a plot of $\frac{i_p}{\nu^{\frac{1}{2}}}$ *vs.* $\nu^{\frac{1}{2}}$ (see Fig. 12c) results in a straight line. From this plot, the values of capacitive ($k^1\nu$) and diffusive ($k^2\nu^{1/2}$) contributions at a scan rate of 5 mV s^{-1} were determined to be approximately 88% and 12%, respectively (Fig. 12d).

© 2024 The Author(s). Published by the Royal Society of Chemistry

Open Access Article. Published on 01 October 2024. Downloaded on 2/13/2026 7:18:18 AM. This article is licensed under a Creative Commons Attribution-NonCommercial 3.0 Unported Licence.

4. Conclusion

In summary, synthesis of a new 1D coordination polymer, $\{[Cu_2(DPP)_2(H_2O)_2]\cdot DPP\cdot 2NO_3\}_n$ (**CP-1**), and its composite (**rGO@CP-1**) was done *via* solvothermal and ball milling approaches, respectively. **CP-1** showed a ***2C1*** underlying net topology. **CP-1** demonstrates excellent selective fluorescence detection capabilities for transition metal ions (Zn^{2+}) and solvents. Furthermore, **CP-1** and its composite (**rGO@CP-1**) exhibited favorable electrochemical energy storage capabilities in 1 M H_2SO_4 electrolytes. However, the composite demonstrates a notable specific capacitance, along with exceptional cycling stability and a low R_{ct} value. So, **CP-1** has potential applications in the detection of selective solvents as well as electrochemical energy storage. Moreover, the composite of **CP-1** could be utilized as a promising electrode material for energy storage.

Author contributions

Basree: writing – original draft, data curation, formal analysis; Waris: electrochemical & formal analysis; A. Ali: writing – origin draft, data curation, conceptualization, methodology, review & editing; N. Khan: formal analysis, data curation; M. Z. Khan: formal & electrochemistry analysis; G. C. Nayak: formal analysis; K. A. Siddiqui: visualization, writing – review & editing; M. Ahmad: supervision, conceptualization, methodology, software, formal analysis, writing – review & editing.

Data availability

Data available on request or similar; supporting information is available in the additional files and further supporting data is available from the authors on request.

Conflicts of interest

The authors declare that they have no known competing financial interests or personal relationships that could have appeared to influence the work reported in this paper.

Acknowledgements

The authors are thankful to the Department of Applied Chemistry, Faculty of Engineering and Technology, Aligarh Muslim University, U.P., India for providing research facilities. Basree is thankful to the DST/INSPIRE Fellowship/2021/IF210635. Waris thanks the UGC for the Non-NET Fellowship. A. Ali also thanks the Institute Post-Doctoral fellowship (DAR/IPDF/CCB/53/2023), Indian Institute of Technology (ISM), Dhanbad. M. A. acknowledges the Start-up grants from the UGC, India.

References

1 E. J. Nixon, A. Jayapaul, R.-J. Chung, S. Rajkumar and J. P. Merlin, *J. Electroanal. Chem.*, 2024, **953**, 118014.
2 H. Liang, Y. Liu, F. Zuo, C. Zhang, L. Yang, L. Zhao, Y. Li, Y. Xu, T. Wang, X. Hua, Y. Zhu and H. Li, *Chem. Sci.*, 2022, **13**, 14191–14197.
3 X. Cao, C. Tan, M. Sindoro and H. Zhang, *Chem. Soc. Rev.*, 2017, **46**, 2660–2677.
4 Y. Ma, L. Zhang, Z. Yan, B. Cheng, J. Yu and T. Liu, *Adv. Energy Mater.*, 2022, **12**, 2103820.
5 T. Sun, L. Xu, D. Wang and Y. Li, *Nano Res.*, 2019, **12**, 2067–2080.
6 H. Bin Wu and X. W. (David) Lou, *Sci. Adv.*, 2017, **3**(12), eaap9252.
7 L. Li, Y. Zheng, S. Zhang, J. Yang, Z. Shao and Z. Guo, *Energy Environ. Sci.*, 2018, **11**, 2310–2340.
8 P. Xiao, F. Bu, R. Zhao, M. F. Aly Aboud, I. Shakir and Y. Xu, *ACS Nano*, 2018, **12**, 3947–3953.
9 J.-H. Yoon, Y. A. Kumar, S. Sambasivam, S. A. Hira, T. N. V. Krishna, K. Zeb, W. Uddin, K. D. Kumar, I. M. Obaidat, S. Kim and H.-J. Kim, *J. Energy Storage*, 2020, **32**, 101988.
10 M. D. Angelin, S. Rajkumar, S. Dhineshkumar, A. T. Ravichandran, A. Ravikumar and J. P. Merlin, *J. Mater. Sci.: Mater. Electron.*, 2023, **34**, 1107.
11 M. Moniruzzaman, Y. Anil Kumar, M. R. Pallavolu, H. M. Arbi, S. Alzahmi and I. M. Obaidat, *Nanomaterials*, 2022, **12**, 3187.
12 Z. Lu, L. Wen, Z. Ni, Y. Li, H. Zhu and Q. Meng, *Cryst. Growth Des.*, 2007, **7**, 268–274.
13 S. Guo, Y. Zhu, Y. Yan, Y. Min, J. Fan, Q. Xu and H. Yun, *J. Power Sources*, 2016, **316**, 176–182.
14 J. Liu, D. Zhu, C. Guo, A. Vasileff and S. Qiao, *Adv. Energy Mater.*, 2017, **7**(23), 1700518.
15 T. Mehtab, G. Yasin, M. Arif, M. Shakeel, R. M. Korai, M. Nadeem, N. Muhammad and X. Lu, *J. Energy Storage*, 2019, **21**, 632–646.
16 Z.-J. Lin, J. Lü, M. Hong and R. Cao, *Chem. Soc. Rev.*, 2014, **43**, 5867–5895.
17 A. J. Howarth, Y. Liu, P. Li, Z. Li, T. C. Wang, J. T. Hupp and O. K. Farha, *Nat. Rev. Mater.*, 2016, **1**, 15018.
18 H.-C. Zhou, J. R. Long and O. M. Yaghi, *Chem. Rev.*, 2012, **112**, 673–674.
19 M. Lippi and M. Cametti, *Coord. Chem. Rev.*, 2021, **430**, 213661.
20 J. Duan, Q. Li and Z. Lu, *CrystEngComm*, 2015, **17**, 2087–2090.
21 V. Jabbari, J. M. Veleta, M. Zarei-Chaleshtori, J. Gardea-Torresdey and D. Villagrán, *Chem. Eng. J.*, 2016, **304**, 774–783.
22 M.-R. Yin, Q.-Q. Yan, B. Li and G.-P. Yong, *CrystEngComm*, 2021, **23**, 3196–3203.
23 Y. K. Hwang, D. Hong, J. Chang, S. H. Jhung, Y. Seo, J. Kim, A. Vimont, M. Daturi, C. Serre and G. Férey, *Angew. Chem.*, 2008, **120**, 4212–4216.
24 S. He, L. Wu, X. Li, H. Sun, T. Xiong, J. Liu, C. Huang, H. Xu, H. Sun, W. Chen, R. Gref and J. Zhang, *Acta Pharm. Sin. B*, 2021, **11**, 2362–2395.
25 Y. Zhang, S. Yuan, G. Day, X. Wang, X. Yang and H.-C. Zhou, *Coord. Chem. Rev.*, 2018, **354**, 28–45.

© 2024 The Author(s). Published by the Royal Society of Chemistry

Open Access Article. Published on 01 October 2024. Downloaded on 2/13/2026 7:18:18 AM. This article is licensed under a Creative Commons Attribution-NonCommercial 3.0 Unported Licence.

26 X. Zhang, W. Wang, Z. Hu, G. Wang and K. Uvdal, *Coord. Chem. Rev.*, 2015, **284**, 206–235.
27 A. Ali, M. Muslim, I. Neogi, M. Afzal, A. Alarifi and M. Ahmad, *ACS Omega*, 2022, **7**, 24438–24451.
28 K. Li, Y. Qin, Z.-G. Li, T.-M. Guo, L.-C. An, W. Li, N. Li and X.-H. Bu, *Coord. Chem. Rev.*, 2022, **470**, 214692.
29 M. Jakoby, C. Beil, P. Nazari, B. S. Richards, M. Seitz, A. Turshatov and I. A. Howard, *iScience*, 2021, **24**, 102207.
30 T. Fan, T. Xia, Q. Zhang, Y. Cui, Y. Yang and G. Qian, *Microporous Mesoporous Mater.*, 2018, **266**, 1–6.
31 N. Levaot and M. Hershfinkel, *Cell Calcium*, 2018, **75**, 53–63.
32 M. Sethupathi, A. Jayamani, G. Muthusankar, P. Sakthivel, K. Sekar, S. Gandhi, N. Sengottuvelan, G. Gopu and C. Selvaraju, *J. Photochem. Photobiol., B*, 2020, **207**, 111854.
33 Y. Huang, Q. Gao, C. Li, X. Chen, X. Li, Y. He, Q. Jin and J. Ji, *Adv. Funct. Mater.*, 2022, **32**, 2109011.
34 V. Sorhie, Alemtoshi, B. Gogoi, B. Walling, S. A. Acharjee and P. Bharali, *Sustainable Chem. Pharm.*, 2022, **30**, 100875.
35 S. Mondal, R. Sahoo and M. C. Das, *Inorg. Chem.*, 2023, **62**, 14124–14133.
36 R. Feyisa Bogale, J. Ye, Y. Sun, T. Sun, S. Zhang, A. Rauf, C. Hang, P. Tian and G. Ning, *Dalton Trans.*, 2016, **45**, 11137–11144.
37 X.-L. Zhao, D. Tian, Q. Gao, H.-W. Sun, J. Xu and X.-H. Bu, *Dalton Trans.*, 2016, **45**, 1040–1046.
38 C. Liu and B. Yan, *Sens. Actuators, B*, 2016, **235**, 541–546.
39 H. Xu, B. Zhai, C.-S. Cao and B. Zhao, *Inorg. Chem.*, 2016, **55**, 9671–9676.
40 P. C. Banerjee, D. E. Lobo, R. Middag, W. K. Ng, M. E. Shaibani and M. Majumder, *ACS Appl. Mater. Interfaces*, 2015, **7**, 3655–3664.
41 R. Deka, V. Kumar, R. Rajak and S. M. Mobin, *Sustainable Energy Fuels*, 2022, **6**, 3014–3024.
42 T. K. Ghosh and G. Ranga Rao, *Dalton Trans.*, 2023, **52**, 5943–5955.
43 G. Cai, P. Cui, W. Shi, S. Morris, S. N. Lou, J. Chen, J. Ciou, V. K. Paidi, K. Lee, S. Li and P. S. Lee, *Adv. Sci.*, 2020, **7**(20), 1903109.
44 A. K. Gupta, M. Saraf, P. K. Bharadwaj and S. M. Mobin, *Inorg. Chem.*, 2019, **58**, 9844–9854.
45 B. S. Stone and R. L. LaDuca, *Polyhedron*, 2014, **81**, 542–549.
46 J. Yu, Z. Wang, X. Luo and H. Du, *Chin. J. Chem.*, 2008, **26**, 1826–1830.
47 G.-G. Luo, H.-B. Xiong and J.-C. Dai, *Cryst. Growth Des.*, 2011, **11**, 507–515.
48 L. Zhao, X. Guan, B. Yu, N. Ding, X. Liu, Q. Ma, S. Yang, A. Yilihamu and S.-T. Yang, *Environ. Int.*, 2019, **133**, 105208.
49 O. V. Dolomanov, L. J. Bourhis, R. J. Gildea, J. A. K. Howard and H. Puschmann, *J. Appl. Crystallogr.*, 2009, **42**, 339–341.
50 L. J. Bourhis, O. V. Dolomanov, R. J. Gildea, J. A. K. Howard and H. Puschmann, *Acta Crystallogr., Sect. A: Found. Adv.*, 2015, **71**, 59–75.
51 X. Zhu, Y. Zhu, S. Murali, M. D. Stoller and R. S. Ruoff, *ACS Nano*, 2011, **5**, 3333–3338.
52 M. Saraf, R. Rajak and S. M. Mobin, *J. Mater. Chem. A*, 2016, **4**, 16432–16445.
53 Somnath, Waris, A. Ali, M. Ahmad and K. A. Siddiqui, *Cryst. Growth Des.*, 2022, **22**, 7374–7394.
54 A. Ali, Waris, Basree, M. Z. Khan, N. Dege, M. Ahmad and M. Shahid, *Dalton Trans.*, 2023, **52**, 15562–15575.
55 E. V. Alexandrov, V. A. Blatov, A. V. Kochetkov and D. M. Proserpio, *CrystEngComm*, 2011, **13**, 3947.
56 V. A. Blatov, A. P. Shevchenko and D. M. Proserpio, *Cryst. Growth Des.*, 2014, **14**, 3576–3586.
57 A. Ali, S. Mishra, S. Kamaal, A. Alarifi, M. Afzal, K. Das Saha and M. Ahmad, *Bioorg. Chem.*, 2021, **106**, 104479.
58 S. S. Mehta, D. Y. Nadargi, M. S. Tamboli, T. Alshahrani, V. R. Minnam Reddy, E. S. Kim, I. S. Mulla, C. Park and S. S. Suryavanshi, *Sci. Rep.*, 2021, **11**, 5023.
59 S. Some, Y. Kim, Y. Yoon, H. Yoo, S. Lee, Y. Park and H. Lee, *Sci. Rep.*, 2013, **3**, 1929.
60 S. Wang, T. Wang, Y. Shi, G. Liu and J. Li, *RSC Adv.*, 2016, **6**, 18465–18470.
61 J.-H. Qin, H.-R. Wang, M.-L. Han, X.-H. Chang and L.-F. Ma, *Dalton Trans.*, 2017, **46**, 15434–15442.
62 A. Li, Z. Hao, C. Han and G. Cui, *Appl. Organomet. Chem.*, 2020, **34**(3), e5313.
63 V. Shukla, M. Ahmad and K. A. Siddiqui, *Mater. Today Chem.*, 2024, **38**, 102138.
64 V. Shukla, M. Ahmad, G. C. Nayak, T. S. Thakur and K. A. Siddiqui, *Cryst. Growth Des.*, 2024, **24**, 3977–3992.
65 W.-J. Gong, R. Yao, H.-X. Li, Z.-G. Ren, J.-G. Zhang and J.-P. Lang, *Dalton Trans.*, 2017, **46**, 16861–16871.
66 X. Zeng, Y. Zhang, J. Zhang, H. Hu, X. Wu, Z. Long and X. Hou, *Microchem. J.*, 2017, **134**, 140–145.
67 F. Yi, J. Li, D. Wu and Z. Sun, *Chem. – Eur. J.*, 2015, **21**, 11475–11482.
68 V. Shukla, M. Ahmad and K. A. Siddiqui, *J. Mol. Struct.*, 2024, **1308**, 138068.
69 J. Chen, F.-Y. Yi, H. Yu, S. Jiao, G. Pang and Z.-M. Sun, *Chem. Commun.*, 2014, **50**, 10506–10509.
70 R. A. Dar, G. A. Naikoo, P. K. Kalambate, L. Giri, F. Khan, S. P. Karna and A. K. Srivastava, *Electrochim. Acta*, 2015, **163**, 196–203.
71 M. Saraf, R. A. Dar, K. Natarajan, A. K. Srivastava and S. M. Mobin, *ChemistrySelect*, 2016, **1**, 2826–2833.
72 M. K. Singh, A. K. Gupta, S. Krishnan, N. Guha, S. Marimuthu and D. K. Rai, *J. Energy Storage*, 2021, **43**, 103301.
73 M. Singh, A. Gupta, P. Saharan, C. Kumar, S. Sundriyal, R. Padhye, T. Daeneke, N. R. Choudhary and S. R. Dhakate, *J. Energy Storage*, 2023, **67**, 107617.
74 R. Rajak, M. Saraf, P. Kumar, K. Natarajan and S. M. Mobin, *Inorg. Chem.*, 2021, **60**, 16986–16995.
75 B. M. Omkaramurthy, G. Krishnamurthy and S. Foro, *SN Appl. Sci.*, 2020, **2**, 342.
76 Z.-X. Li, B.-L. Yang, K.-Y. Zou, L. Kong, M.-L. Yue and H.-H. Duan, *Carbon*, 2019, **144**, 540–548.
77 M. K. Singh, A. K. Gupta, S. Krishnan, N. Guha, S. Marimuthu and D. K. Rai, *J. Energy Storage*, 2021, **43**, 103301.
78 J. Liu, Y. Zhou, Z. Xie, Y. Li, Y. Liu, J. Sun, Y. Ma, O. Terasaki and L. Chen, *Angew. Chem., Int. Ed.*, 2020, **59**, 1081–1086.

© 2024 The Author(s). Published by the Royal Society of Chemistry

Open Access Article. Published on 01 October 2024. Downloaded on 2/13/2026 7:18:18 AM.
This article is licensed under a Creative Commons Attribution-NonCommercial 3.0 Unported Licence.

79 S. Rajkumar, E. Elanthamilan, J. P. Merlin, I. J. Daisy Priscillal and I. S. Lydia, *Sustainable Energy Fuels*, 2020, **4**, 5313–5326.
80 A. M. Afzal, N. Muzaffar, M. W. Iqbal, G. Dastgeer, A. Manzoor, M. Razaq, S. M. Wabaidur, E. A. Al-Ammar and S. M. Eldin, *J. Appl. Electrochem.*, 2024, **54**, 65–76.
81 K. Wang, Z. Wang, X. Wang, X. Zhou, Y. Tao and H. Wu, *J. Power Sources*, 2018, **377**, 44–51.
82 S. Rajkumar, S. Gowri, S. Dhineshkumar, J. P. Merlin and A. Sathiyan, *New J. Chem.*, 2021, **45**, 20612–20623.
83 I. Ahmad and A. Kumar, *Chem. Eng. J.*, 2023, **477**, 146972.
84 R. Sahoo, D. T. Pham, T. H. Lee, T. H. T. Luu, J. Seok and Y. H. Lee, *ACS Nano*, 2018, **12**, 8494–8505.